



**Coupled-mode theory of the polarization dynamics inside a microring resonator with a uniaxial core**Luis Cortes-Herrera,<sup>\*</sup> Xiaotong He, Jaime Cardenas , and Govind P. Agrawal *The Institute of Optics, University of Rochester, Rochester, New York 14627, USA*

(Received 11 December 2020; accepted 8 June 2021; published 22 June 2021)

The use of a uniaxial birefringent material such as lithium niobate ( $\text{LiNbO}_3$ , LN) as the core of a microring resonator leads to coupling between transverse-electric and transverse-magnetic modes. We develop a theoretical framework to study polarization evolution inside such a resonator. We write Maxwell's equations in the form of a Schrödinger equation and use it to obtain coupled-mode equations modeling the continuous reorientation of the optic axis as light propagates inside the microring resonator. We show that the mode-coupling problem is isomorphic to a quantum-mechanical two-level system modulated in frequency and driven by a classical optical field. We analyze the polarization coupling by using the well-known techniques of quantum mechanics such as time-dependent perturbation theory, the rotating-wave approximation, and the adiabatic approximation. As an example, we consider a LN ring resonator and describe the evolution of the state of polarization of injected light along the ring's circumference.

DOI: [10.1103/PhysRevA.103.063517](https://doi.org/10.1103/PhysRevA.103.063517)**I. INTRODUCTION**

Microring resonators have attracted attention for over a decade due to their diverse applications, with optical frequency combs being one example [1–3]. Recently, lithium niobate ( $\text{LiNbO}_3$ , LN), a uniaxial dielectric, has been used to fabricate such resonators because of its excellent electro-optic properties [4–7]. It has been noticed that the material birefringence of LN couples the transverse-electric (TE) and transverse-magnetic (TM) modes in a microring resonator [8], resulting in unusual polarization dynamics that are not yet fully understood. The objective of this paper is to develop a theory for the polarization evolution in LN-based microring resonators.

Modes of uniaxial planar waveguides have been studied for over forty years [9–14]. It has been found that the mode hybridization depends on the relative orientation of the optic axis with respect to the plane of the core layer and the direction of propagation. Of course, even an isotropic planar waveguide exhibits geometric birefringence due to the difference in the effective refractive indexes of its TE and TM modes. When an anisotropic material is used to form a planar waveguide, the modal birefringence is determined by a combination of both geometric and material properties. In a microring resonator, the curvature of the ring waveguide leads to additional complication when the optic axis of the material lies in the plane of the core layer. In this case, the angle between the optic axis and the direction of propagation varies continuously as light propagates along the ring. In general, this continuous rotation complicates the polarization evolution of the guided radiation. We have developed a simple theoretical approach to model the polarization dynamics resulting from the curvature of a uniaxial microring resonator.

The paper is organized as follows: In Sec. II, we provide an intuitive description of the physics governing the polarization-mode dynamics and introduce the zero-bending model, which replaces the ring waveguide with a straight waveguide in which the optic axis changes continuously. In Sec. III, we leverage this model to develop a coupled-mode theory for the TE and TM modes of a microring resonator. In Sec. IV, we determine the coupling matrix due to the continuous optic axis reorientation and discuss the effect of polarization coupling on the resonances of a microring resonator. In Sec. V, we approximate the modes with those of a slab waveguide and demonstrate that the resulting polarization dynamics are isomorphic to those of a frequency-modulated two-level atom driven by a classical optical field. We exploit this analogy and study polarization coupling in a microring resonator using well-known techniques and concepts of quantum mechanics such as time-dependent perturbation theory, the rotating-wave approximation, and adiabatic following. In Sec. VI, we demonstrate the usefulness of our theory by applying it to the case of a LN waveguide with a silica ( $\text{SiO}_2$ ) substrate and air cladding. In Sec. VII, we summarize our results.

**II. INTUITIVE DESCRIPTION AND THE ZERO-BENDING MODEL**

We consider a microring resonator of radius  $r$ , as sketched in Fig. 1. A straight bus waveguide is used to inject light into this resonator at the location where the ring comes closest to the bus waveguide. Generally, the injected light excites a coherent sum of the TE and TM modes of the ring waveguide, depending on its state of polarization (SOP). The core of the ring waveguide is made of a uniaxial anisotropic material. The extraordinary (optic) axis of this uniaxial material lies in the plane of the ring in a fixed direction  $\hat{u}_e$  (see Fig. 1). As the injected light travels along the ring, sweeping the arc

<sup>\*</sup>lcortesh@ur.rochester.edu

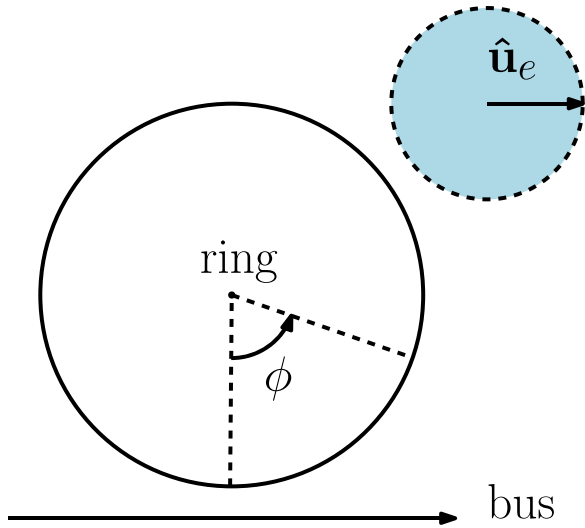


FIG. 1. A microring resonator and the orientation of its optic axis  $\hat{\mathbf{u}}_e$ .

angle  $\phi$ , its SOP changes continuously. This occurs because the relative angle between the optic axis and the direction of propagation varies along the ring.

To understand the evolution of the SOP, one may examine the components of the permittivity dyadic  $\vec{\epsilon}$  of the guiding core in a coordinate frame rotating with the ring waveguide. In this rotating frame, the diagonal components of  $\vec{\epsilon}$  oscillate, causing an analogous oscillation in the effective indices of the local guided modes. In the rotating frame, the permittivity also develops nondiagonal components, also oscillating in magnitude along the ring. If these nondiagonal elements link electric-field components of different guided modes, these become locally coupled and exchange energy. This intuitive description will be given mathematical precision in the sections that follow.

The analysis of light propagation even in an isotropic curved waveguide is known to be challenging [15]. Adding material anisotropy to such a waveguide makes the problem even more difficult. It is then desirable to find an equivalent formulation that preserves the fundamental physics. For this purpose, we propose the “zero-bending model” (ZBM), illustrated by Fig. 2. Effectively, the ZBM replaces the curved waveguide with a straight waveguide along which the extraordinary axis rotates continuously with propagation distance  $z$  forming a rotation angle  $\phi = z/r$ . At a distance  $z = 2\pi r$ , corresponding to one round trip inside the microring resonator,

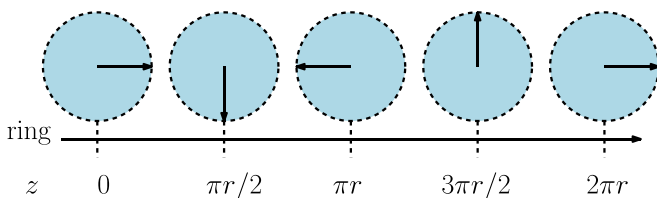


FIG. 2. Rotation of the optic axis in the zero-bending model (ZBM) that replaces the curved waveguide with a straight waveguide.

the optic axis returns to the initial orientation, so the ZBM waveguide is periodic along  $z$  with a period  $2\pi r$ .

The mathematical simplification afforded by the ZBM comes at a cost. This consists of the neglect of any effect of the finite curvature of the ring on light propagation other than the continuous reorientation of the optic axis. The most prominent among the neglected effects are the bending loss and the field displacement [15]. The impact of these two effects scales with the ring’s curvature. Hence, we expect the results obtained via the ZBM to be accurate when the ring radius  $r$  is large compared with both the wavelength of light  $\lambda$  and the characteristic dimension  $d$  of the waveguide’s cross section. This conclusion follows from dimensional analysis, as these are the only other characteristic lengths of the problem, and has been proven to be correct for isotropic bent waveguides [15]. Both conditions,  $r \gg \lambda$  and  $r \gg d$ , are usually satisfied in practice, indicating that our ZBM-based description is applicable to most experimental situations. Of course, higher index contrast between the ring core and substrate results in lower bending losses. So we expect the ZBM to be more accurate in higher-contrast microrings, all else being equal.

### III. COUPLED-MODE FORMALISM

Adopting the ZBM, we analyze light propagation in a straight birefringent waveguide oriented along the direction of propagation  $\hat{\mathbf{z}}$ . As usual, Maxwell’s equations are the starting point of our coupled-mode theory (CMT). Following earlier work [16,17], we write Maxwell’s equations in the form of a Schrödinger equation. This has the advantage of immediately yielding orthogonality relations for the guided modes and facilitating the formulation of a CMT, even for an anisotropic waveguide.

For this formulation, we decompose all field vectors into parts that are transverse and parallel to the direction of propagation,  $\hat{\mathbf{z}}$ . Similarly, the relative permittivity dyadic  $\vec{\epsilon}$  is decomposed as [18]

$$\vec{\epsilon} = \vec{\epsilon}_t + \epsilon_z \hat{\mathbf{z}}\hat{\mathbf{z}} + \vec{\epsilon}_{tz} \hat{\mathbf{z}} + \hat{\mathbf{z}}\vec{\epsilon}_{zt}, \quad (1)$$

where  $\vec{\epsilon}_t$  is a transverse dyadic,  $\epsilon_z$  is a scalar and both  $\vec{\epsilon}_{tz}$  and  $\vec{\epsilon}_{zt}$  are transverse vectors. In this paper, the juxtaposition of two vectors indicates a tensor product.

Assuming the time dependence  $\exp(-i\omega t)$  for all electromagnetic fields and using Eq. (1), we write the two curl equations of Maxwell in the form of a single Schrödinger equation, with  $z$  playing the role of time. In Dirac notation this equation is written as [16,17]

$$-i \frac{\partial}{\partial z} \hat{\mathbf{B}}|\psi\rangle = \hat{\mathbf{A}}|\psi\rangle, \quad (2)$$

where  $|\psi\rangle$  specifies the optical field in a plane transverse to  $\hat{\mathbf{z}}$  and is related to the transverse electric and magnetic fields,  $\mathbf{E}_t$  and  $\mathbf{H}_t$ , by

$$|\psi\rangle \equiv \begin{pmatrix} \sqrt{\epsilon_0} \mathbf{E}_t \\ \sqrt{\mu_0} \mathbf{H}_t \end{pmatrix}. \quad (3)$$

As usual,  $\epsilon_0$  and  $\mu_0$  stand for the electric permittivity and the magnetic permeability of vacuum, respectively, and their

square roots are included so that all components of  $|\psi\rangle$  share the same units.

In Eq. (2),  $\hat{B}$  and  $\hat{A}$  are two linear operators of the form

$$\hat{B} = \begin{pmatrix} 0 & -\hat{\mathbf{z}} \times \\ \hat{\mathbf{z}} \times & 0 \end{pmatrix}, \quad \hat{A} = \begin{pmatrix} \hat{A}_{ee} & \hat{A}_{eh} \\ \hat{A}_{he} & \hat{A}_{hh} \end{pmatrix}. \quad (4)$$

Here,  $\hat{A}_{ee}$ ,  $\hat{A}_{eh}$ ,  $\hat{A}_{he}$ , and  $\hat{A}_{hh}$  are operators that map the vector space of transverse fields onto itself. They depend on the components of  $\vec{\epsilon}$  as

$$\begin{aligned} \hat{A}_{ee} &= k_0 \left( \frac{\vec{\epsilon}_t}{\epsilon_t} - \frac{\vec{\epsilon}_{tz} \vec{\epsilon}_{zt}}{\epsilon_z} \right) - k_0^{-1} \nabla_t \times \nabla_t \times, \\ \hat{A}_{eh} &= i \left( \frac{\vec{\epsilon}_{tz} \hat{\mathbf{z}}}{\epsilon_z} \right) \cdot (\nabla_t \times), \\ \hat{A}_{he} &= -i \nabla_t \times \left( \frac{\hat{\mathbf{z}} \vec{\epsilon}_{z,t}}{\epsilon_z} \right), \\ \hat{A}_{hh} &= k_0 - k_0^{-1} \nabla_t \times \left( \frac{1}{\epsilon_z} \nabla_t \times \right), \end{aligned} \quad (5)$$

where  $\nabla_t \times$  is the transverse curl operator,  $k_0 \equiv \omega/c$ , and  $c$  is the speed of light in vacuum.

To exploit the mathematical machinery of quantum mechanics, the inner product of the two states  $|\psi_a\rangle$  and  $|\psi_b\rangle$  needs to be defined. We define it as the positive-definite quadratic form [16]

$$\langle \psi_a | \psi_b \rangle \equiv \frac{1}{4} \iint (\eta_0^{-1} \mathbf{E}_{ta}^* \cdot \mathbf{E}_{tb} + \eta_0 \mathbf{H}_{ta}^* \cdot \mathbf{H}_{tb}) dx dy, \quad (6)$$

where  $\eta_0 = \sqrt{\mu_0/\epsilon_0}$  is the impedance of vacuum. Both operators  $\hat{A}$  and  $\hat{B}$  are Hermitian under the inner product (6) for localized fields like those of guided modes [17]. The definition in Eq. (6) has the additional property that  $\langle \psi | \hat{B} | \psi \rangle$  gives the time-averaged power carried by  $|\psi\rangle$  along  $z$ .

We can use Eq. (2) to characterize the guided modes of a longitudinally invariant waveguide. Since the  $z$  dependence of a propagation mode,  $|\beta\rangle$ , is  $\exp(i\beta z)$  for some propagation constant  $\beta$ , each mode satisfies

$$\beta \hat{B} |\beta\rangle = \hat{A} |\beta\rangle. \quad (7)$$

As recognized in Ref. [16], Eq. (7) is a generalized eigenvalue equation for the operator pair  $\{\hat{A}, \hat{B}\}$ , with the eigenvalue  $\beta$  and the eigenvector  $|\beta\rangle$ .

Given Eq. (7) and that both  $\hat{A}$  and  $\hat{B}$  are Hermitian operators, all off-diagonal matrix elements  $\langle \beta | \hat{B} | \beta' \rangle$  vanish for  $\beta' \neq \beta^*$  [19]. Furthermore, all eigenvalues are real for modes carrying nonzero power [16]. So, if we treat only copropagating guided modes and normalize them so they carry unit power along  $z$ , we get the orthonormality relation

$$\langle \beta | \hat{B} | \beta' \rangle = \delta_{\beta, \beta'}, \quad (8)$$

where  $\delta_{\beta, \beta'}$  equals 1 if  $\beta = \beta'$  and 0 otherwise.

Given the relations (7) and (8), we employ the mathematics of quantum-mechanical time-dependent perturbation theory to develop a CMT for birefringent waveguides. In this approach, the state  $|\psi(z)\rangle$  is approximated as a coherent superposition of the normal modes  $|\beta_n\rangle$  even when the operator

$\hat{A}$  becomes a  $z$ -dependent operator  $\hat{A}'(z)$  in Eq. (2):

$$|\psi(z)\rangle = \sum_n \tilde{a}_n(z) |\beta_n\rangle. \quad (9)$$

Of course, this approximation is valid only when the difference between  $\hat{A}'(z)$  and  $\hat{A}$  is relatively small.

Substituting this expansion in Eq. (2) [with  $\hat{A}'(z)$  instead of  $\hat{A}$ ] and making use of the orthonormality relation (8), we obtain the following set of coupled equations for the mode amplitudes  $\tilde{a}_n(z)$ :

$$-i \frac{d\tilde{a}_n}{dz} = \beta_n \tilde{a}_n + \sum_m D_{nm}(z) \tilde{a}_m, \quad (10)$$

where  $D_{nm}(z) \equiv \langle \beta_n | \hat{D}(z) | \beta_m \rangle$  are the matrix elements of the perturbation operator  $\hat{D}(z) \equiv \hat{A}'(z) - \hat{A}$ . We use these coupled-mode equations in the next section to study TE-TM mode coupling in a microring resonator.

If we wished to forgo the ZBM, we could write Maxwell's equations in cylindrical coordinates and consider propagation of the optical field along the azimuthal coordinate. In this case, the decomposition of  $\vec{\epsilon}$  in Eq. (1) would need to single out the azimuthal component, rather than one along  $z$ . The main theoretical difficulty in such a formulation arises from the well-known fact that the propagation constant  $\beta$  becomes complex, on account of bending loss [20]. This implies that the analog of operator  $\hat{A}$  is not Hermitian and the orthogonality relations (8) need no longer hold for bent waveguides. Although orthogonality relations have been obtained for bent waveguides with simplified geometries [21,22], the presence of bending loss prohibits the formulation of orthogonality relations for a general waveguide cross section. Of course, one may decide to neglect bending losses and treat  $\hat{A}$  as approximately Hermitian, and, as a result, have Eq. (8) hold as an approximation. In such a case, however, the ZBM should be accurate and result in simpler calculations.

## IV. POLARIZATION COUPLING IN THE ZERO-BENDING MODEL

### A. Perturbation due to permittivity reorientation

Equation (10) describes how the mode amplitudes  $\tilde{a}_n(z)$  are coupled through the dielectric perturbation  $\hat{D}(z) = \hat{A}'(z) - \hat{A}$ . The next step is to find an expression for  $\hat{D}(z)$ . For both the unperturbed and perturbed systems, the permittivity is a symmetric dyadic with a value  $n_o^2$  along the two ordinary axes and  $n_e^2$  along the extraordinary (optic) axis. For the unperturbed system, we take the optic axis along the  $z$  axis. This orientation matches  $\phi = 0$  in Fig. 1 and  $z = 0$  in Fig. 2. With this choice, the unperturbed basis modes are TE- and TM-polarized modes; this identification aids subsequent physical interpretation. In the perturbed system, the optic axis rotates on the  $x$ - $z$  plane, forming the angle  $\phi = z/r$  with respect to the  $z$  axis, as depicted in Fig. 2.

Based on this description, we write the core's unperturbed and perturbed permittivities,  $\vec{\epsilon}$  and  $\vec{\epsilon}'$ , as

$$\begin{aligned} \vec{\epsilon} &= n_o^2 (\hat{\mathbf{x}}\hat{\mathbf{x}} + \hat{\mathbf{y}}\hat{\mathbf{y}}) + n_e^2 \hat{\mathbf{z}}\hat{\mathbf{z}}, \\ \vec{\epsilon}'(\phi) &= n_o^2 (\hat{\mathbf{u}}_o(\phi) \hat{\mathbf{u}}_o(\phi) + \hat{\mathbf{y}}\hat{\mathbf{y}}) + n_e^2 \hat{\mathbf{u}}_e(\phi) \hat{\mathbf{u}}_e(\phi), \end{aligned} \quad (11)$$

where the unit vectors  $\hat{\mathbf{u}}_o(\phi)$  and  $\hat{\mathbf{u}}_e(\phi)$  are given by

$$\begin{aligned}\hat{\mathbf{u}}_o(\phi) &= \cos \phi \hat{\mathbf{x}} + \sin \phi \hat{\mathbf{z}}, \\ \hat{\mathbf{u}}_e(\phi) &= -\sin \phi \hat{\mathbf{x}} + \cos \phi \hat{\mathbf{z}}.\end{aligned}\quad (12)$$

We substitute Eq. (11) into Eq. (5) to evaluate both  $\hat{A}$  and  $\hat{A}'$  and use them to write the perturbation  $\hat{D}$  in the form

$$\hat{D}(z) = \sum_{n=1}^3 \hat{D}^{(n)} f_n(\phi, \zeta), \quad (13)$$

where  $\zeta \equiv (n_e^2 - n_o^2)/(n_e^2 + n_o^2)$  is a measure of the guiding core's material birefringence and  $\hat{D}^{(n)}$  are  $z$ -independent Hermitian operators defined as

$$\begin{aligned}\hat{D}^{(1)} &= \begin{pmatrix} k_0 \bar{\epsilon} C(x, y) \hat{\mathbf{x}} \hat{\mathbf{x}} & 0 \\ 0 & 0 \end{pmatrix}, \\ \hat{D}^{(2)} &= \begin{pmatrix} 0 & -iC(x, y) \hat{\mathbf{x}} \hat{\mathbf{z}} \cdot (\nabla_t \times) \\ i \nabla_t \times [\hat{\mathbf{z}} \hat{\mathbf{x}} C(x, y)] & 0 \end{pmatrix}, \\ \hat{D}^{(3)} &= \begin{pmatrix} 0 & 0 \\ 0 & (k_0 \bar{\epsilon})^{-1} \nabla_t \times [C(x, y) \nabla_t \times] \end{pmatrix}.\end{aligned}\quad (14)$$

Here,  $\bar{\epsilon} = (n_e^2 + n_o^2)/2$  and  $C(x, y)$  is a generalized function (or distribution) which equals unity inside the waveguide's cross section and zero outside of it. The scalar functions  $f_n(\phi, \zeta)$  in (13) depend on  $z = r\phi$  through

$$\begin{aligned}f_1(\phi, \zeta) &= \zeta(1 - \cos 2\phi) - \zeta^2 f(\phi, \zeta) \sin^2 2\phi, \\ f_2(\phi, \zeta) &= \zeta f(\phi, \zeta) \sin 2\phi, \\ f_3(\phi, \zeta) &= (1 + \zeta)^{-1} - f(\phi, \zeta),\end{aligned}\quad (15)$$

where the auxiliary function  $f(\phi, \zeta)$  is defined as

$$f(\phi, \zeta) \equiv (1 + \zeta \cos 2\phi)^{-1}. \quad (16)$$

Equations (13) to (16) indicate that the  $z$  dependence of  $\hat{D}(z)$  comes only from the  $\phi$  dependence of the scalars  $f_n(\phi, \zeta)$ , which are periodic in  $\phi = z/r$  with a period of  $\pi$ . Therefore,  $\hat{D}(z)$  is periodic in  $z$  with period  $\pi r$ . This agrees with physical intuition, as the ring in Fig. 1 is invariant when rotated by 180 degrees around the axis normal to the plane of propagation.

In Fig. 1, we assumed the bus waveguide to be aligned with the optic axis, so it was natural to define  $\phi = 0$  at the point on the ring closest to the bus. In practice, one could have the bus perpendicular to the optic axis, as the bus would still possess independent TE and TM modes. Of course, our analysis can still be applied to such a configuration. The net effect is that formulas (13) to (16) still apply, provided the birefringence parameter  $\zeta$  is replaced with  $-\zeta$ . In Fig. 1, we also assumed that light is injected into the bus from the left side, so that it travels counterclockwise along the ring. Our analysis can also be used when light is injected from the right side and travels clockwise inside the ring. It is easy to verify that Eqs. (13) to (16) can still be used if we replace  $\phi$  with  $-\phi$ . If the bus is perpendicular to the optic axis and light travels clockwise inside the ring, one needs to replace both  $\zeta$  with  $-\zeta$  and  $\phi$  with  $-\phi$ .

## B. Resonance condition for microring resonators

In Sec. III, we found that the mode amplitudes  $\tilde{a}_n(z)$  satisfy the coupled-mode equations (10). These equations can be solved to find the field amplitudes at any point  $z = r\phi$  along the ring, if we know their values at some  $z_0 = r\phi_0$ . Because the coupled-mode equations are linear, we can write their solution in the form

$$\tilde{a}(z) = \tilde{U}(\phi, \phi_0) \tilde{a}(\phi_0), \quad (17)$$

where  $\tilde{a}(\phi)$  is a column vector whose  $n$ th element equals  $\tilde{a}_n(\phi)$  and  $\tilde{U}(\phi, \phi_0)$  is a square matrix. The evolution matrix  $\tilde{U}(\phi, \phi_0)$  is unitary because the propagation constants  $\beta_n$  are real and the perturbation operator  $\hat{D}(z)$  is Hermitian. As is well known, a unitary matrix has a complete set of orthonormal eigenvectors and all its eigenvalues have unit magnitude.

The microring's resonance frequencies are implicitly determined by the round-trip matrix  $\tilde{U}(2\pi, 0)$ , which maps the initial amplitudes  $\tilde{a}(0)$  to those obtained after one round trip around the ring. To see this, observe that the eigenvectors of  $\tilde{U}(2\pi, 0)$  represent the polarization states that reproduce themselves after each round trip up to a phase factor equal to the corresponding eigenvalue. If this eigenvalue equals one, the eigenstate reproduces itself exactly after a round trip, i.e.,  $\tilde{a}(2\pi) = \tilde{a}(0)$ . This is the resonance condition. Recall that  $\hat{D}(z)$  depends on frequency through the wave number  $k_0 \equiv \omega/c$  in Eq. (14), and consequently so does  $\tilde{U}(2\pi, 0)$ . Hence, there exists a discrete set of values of the frequency  $\omega$  for which one of the eigenvalues of  $\tilde{U}(2\pi, 0)$  equals one. These values of  $\omega$  constitute the resonance frequencies of the microring resonator. Because coupling between the TE and TM modes changes the eigenvalues of  $\tilde{U}(2\pi, 0)$ , we expect this coupling to shift the ring's resonance frequencies.

## V. APPROXIMATE ANALYTIC SOLUTION OF COUPLE-MODE EQUATIONS

### A. Simplification of the coupled-mode equations

Given the form of the perturbation operator  $\hat{D}$  in Eq. (13), the coupled-mode equations (10) in general must be solved numerically. In theory, one could leverage the periodicity of  $\hat{D}(z)$  to employ Floquet theory [23]. However, this approach obscures the physics and still requires new approximations, like the truncation of an infinite Fourier series. In this section we find approximate analytical solutions to Eqs. (10) after introducing suitable simplifications.

The approximations we make are as follows: First, we assume that the originally unbent ring waveguide (the unperturbed waveguide in the ZBM) either supports only fundamental TE and TM modes or only these two modes are excited by the light injected into the ring. Even in the presence of higher-order modes, this assumption holds if the difference between the effective indices of different order is sufficiently large that coupling between them is phase-mismatched. For brevity, we follow convention and denote the fundamental TE and TM modes by  $s$  and  $p$ , respectively.

Second, we assume that the material anisotropy is small, so the anisotropy parameter  $\zeta$  satisfies  $|\zeta| \ll 1$  and we can expand  $f_n(\phi, \zeta)$  in Eq. (13) in a power series in  $\zeta$  and retain only terms up to the first order. This assumption is consistent

with the use of CMT and usually holds in practice. For example,  $|\zeta| = 0.032$  for a LN waveguide at wavelengths near 1550 nm [8].

Third, we assume that the cross section of the ring waveguide is such that its one dimension is much larger than the other one, i.e., the modes are strongly confined only along one dimension. Hence, we may approximate the waveguide cross-section as one dimensional by taking the larger dimension as infinite. These assumptions facilitate numerical calculations and reduce the number of free parameters in the problem.

Next we examine again the geometry of the ring waveguide in Fig. 2, where both the ring and the optic axis lie in the  $x$ - $z$  plane and the  $y$  axis is normal to this plane. To approximate the waveguide cross section as one dimensional, we could extend it infinitely in either the  $x$  or  $y$  direction. If the waveguide is kept narrow in the  $x$  direction but is much thicker in the  $y$  direction, we call it an out-of-plane slab waveguide. If the waveguide is relatively thin but much wider in the  $x$  direction, we refer to as an in-plane slab. We find that these two configurations behave quite differently from the standpoint of mode coupling.

It can be shown [24] that the matrix element  $D_{sp}(z)$  vanishes for the out-of-plane slab waveguide, indicating that the  $s$  and the  $p$  modes do not couple in such waveguides. In fact, the only effect of the permittivity reorientation is a shift of the propagation constant for the  $p$  mode. This agrees with previous theoretical investigations of the normal modes of such slab waveguides [27]. In contrast, the  $s$  and the  $p$  modes generally undergo coupling for in-plane slab waveguides. Thus, unless otherwise stated, we focus subsequent analysis only on in-plane waveguides which width is much larger than their thickness. This is also often the case in practice, so the in-plane waveguide is the configuration of technological interest, too.

This distinction between the coupling behavior of in-plane and out-of-plane waveguides can be understood by analyzing the electric-field components of the guided modes for each waveguide geometry. The electric field of the TE mode of the in-plane waveguide lies in the plane of propagation. So does the longitudinal electric field of its TM mode. These two fields are coupled by the anisotropic permittivity dyadic because it possesses nondiagonal components mapping transverse fields to longitudinal ones and vice versa. In contrast, the out-of-plane waveguide has the electric field of its TE mode normal to the plane of propagation. Rotation of the direction of propagation relative to the in-plane optic axis cannot result in nondiagonal permittivity elements mapping this TE field into the plane. Consequently, in an out-of-plane waveguide, a TE mode cannot couple to a TM mode, whose electric field lies completely in the plane of propagation.

We should also mention that the TE-TM mode coupling depends on whether the in-plane waveguide's cladding and substrate (assumed isotropic) have the same or different refractive indexes. If these indexes are the same (symmetric case), the TE (TM) modes have definite spatial parity and even orders couple only to TM (TE) modes of odd orders [24]. If such a waveguide supports only fundamental modes, no coupling occurs between its TE- and TM-polarized modes to the accuracy of CMT. If the cladding and substrate refractive indexes differ (asymmetric case), however, the modes

no longer have definite parity so the fundamental TE- and TM-modes couple.

### B. Analysis of the simplified coupled-mode equations

With the preceding simplifications, the amplitude vector  $\tilde{a}(\phi)$  becomes two dimensional with elements  $\tilde{a}_s(\phi)$  and  $\tilde{a}_p(\phi)$  and can be interpreted as a Jones vector. Of course, one should be careful with this interpretation because the guided modes possess nonhomogeneous spatial distributions and longitudinal components due to mode confinement. In addition, each polarization mode is normalized to carry unit power, rather than keeping a constant intensity ratio at any point in space. Hence, the electric field generally does not trace the traditional polarization ellipse, as in plane-wave optics.

Consider next the matrix elements  $D_{nm}^{(l)}$  of the operators  $\hat{D}^{(l)}$  ( $l = 1, 2, 3$ ) with  $n, m$  taking values  $s$  or  $p$ . As proved in Ref. [24] for the in-plane geometry, only four of the twelve possible matrix elements are nonvanishing. These are  $D_{ss}^{(1)}$ ,  $D_{sp}^{(2)}$ ,  $D_{ps}^{(2)} = [D_{sp}^{(2)}]^*$ , and  $D_{pp}^{(3)}$ . Also,  $D_{ss}^{(1)}$  and  $D_{pp}^{(3)}$  are purely real because the matrices  $D^{(l)}$  are Hermitian.

To further simplify the problem, we introduce a new column vector  $a(\phi)$  via

$$\tilde{a}(\phi) = \exp[i\theta(\phi)]a(\phi), \quad (18)$$

where  $\theta(\phi)$  is the common phase acquired by  $\tilde{a}(\phi)$  during propagation along the ring:

$$\theta(\phi) = \frac{1}{2}r(\beta_s + \beta_p)\phi + \frac{1}{2}r\zeta(D_{ss}^{(1)} - D_{pp}^{(3)})(\phi - \frac{1}{2}\sin 2\phi), \quad (19)$$

where we have performed a small  $\zeta$  truncation, as discussed in Sec. V A.

Then, setting  $\phi = z/r$  as the independent variable, the coupled-mode equations become

$$-i\frac{da}{d\phi} = H(\phi)a, \quad (20)$$

where  $H(\phi)$  is a  $\phi$ -dependent  $2 \times 2$  matrix, akin to a time-dependent Hamiltonian in quantum mechanics. It may be written in terms of the Pauli spin matrices  $\sigma_n$  ( $n = 1, 2, 3$ ) as

$$H(\phi) = \frac{1}{2}(\Delta_0 + \Delta_1 \cos 2\phi)\sigma_1 + (\kappa \sin 2\phi)\sigma_3, \quad (21)$$

where

$$\sigma_1 = \begin{pmatrix} 1 & 0 \\ 0 & -1 \end{pmatrix}, \quad \sigma_2 = \begin{pmatrix} 0 & 1 \\ 1 & 0 \end{pmatrix}, \quad \sigma_3 = \begin{pmatrix} 0 & -i \\ i & 0 \end{pmatrix}. \quad (22)$$

We follow optics convention [34,35] and label the Pauli matrices so that the Stokes parameters  $S_n$  are obtained through  $S_n = a^\dagger \sigma_n a$ .

In Eq. (21), we introduced three parameters that govern polarization dynamics of the microring. These are the ring-averaged detuning  $\Delta_0$ ; the detuning-oscillation amplitude  $\Delta_1$ ; and the coupling coefficient  $\kappa$ . The three parameters can be explicitly evaluated from the relations

$$\begin{aligned} \Delta_0 &= r(\beta_s - \beta_p) - \Delta_1, \\ \Delta_1 &= -r\zeta(D_{ss}^{(1)} + D_{pp}^{(3)}), \\ \kappa &= -r\zeta\Im\{D_{sp}^{(2)}\}, \end{aligned} \quad (23)$$

where, naturally,  $\beta_s$  and  $\beta_p$  are the propagation constants of the unperturbed  $s$  and  $p$  modes, respectively.

Expressions (20) and (21) constitute the main result of this section. They describe how the amplitudes of TE and TM modes evolve along a microring resonator with the angle  $\phi$ . These equations are mathematically equivalent to those governing a frequency-modulated two-level atom driven by a classical optical field [30]. The first term, proportional to  $\sigma_1$ , represents a local mode detuning that oscillates between  $(\Delta_0 - \Delta_1)$  and  $(\Delta_0 + \Delta_1)$  along the ring. The last term represents polarization coupling whose magnitude oscillates between  $-\kappa$  and  $\kappa$ . As shown later, the combination of these two effects leads to complicated polarization dynamics on the Poincaré sphere.

We find that the form of the matrix  $H(\phi)$  in Eq. (21) agrees with the intuitive description of polarization coupling in Sec. II. The oscillation of its diagonal term, modeling local detuning, is a consequence of the oscillation in the diagonal components of the permittivity in the frame rotating with the ring waveguide. Observe that the detuning extrema occur when  $\phi$  is an integer multiple of  $\pi/2$ , when the direction of propagation is either parallel or perpendicular to the optic axis, so the diagonal permittivity elements are themselves extremized. On the other hand, the oscillation of the nondiagonal term of  $H(\phi)$ , proportional to  $\sigma_3$ , occurs due to the oscillation of the nondiagonal permittivity elements in the rotating frame. Thus, mode coupling is strongest when  $\phi$  is an odd multiple of  $\pi/4$ , just where the nondiagonal permittivity elements are extremized.

Note that  $H(\phi)$  varies in the three-dimensional parameter space spanned by  $\Delta_0$ ,  $\Delta_1$ , and  $\kappa$ . Since  $H(\phi)$  alone governs the polarization dynamics in Eq. (20), the polarization dynamics also vary in this space. Generally, Eq. (20) must be solved numerically. Nonetheless, approximate analytic solutions can be obtained in certain regions of the parameter space by employing analytic tools for quantum systems with a time-dependent Hamiltonian [36]. In the following sections, we discuss these approximate solutions and their regions of validity.

Again, because Eq. (20) is linear with the Hermitian  $H(\phi)$ , we may write its solution as  $a(\phi) = U(\phi, 0)a(0)$ , where  $U(\phi, 0)$  is unitary and satisfies

$$-i \frac{dU}{d\phi} = H(\phi)U(\phi, 0), \quad (24)$$

with the initial condition  $U(0, 0) = 1$ . Of course, we may relate this  $U(\phi, 0)$  to the full round-trip matrix  $\tilde{U}(\phi, 0)$  of Sec. IV B through the relation

$$\tilde{U}(\phi, 0) = \exp[i\theta(\phi)]U(\phi, 0), \quad (25)$$

with  $\theta(\phi)$  given by (19). In what follows, we provide approximate expressions for  $U(\phi, 0)$  and investigate its properties and the corresponding polarization eigenstates of the ring.

### C. Perturbative regime

One way to solve Eq. (24) approximately is using a perturbative approach. As is known from quantum mechanics [36], this type of solution is accurate when  $H(\phi)$  can be written as  $H = H_0 + V$ , where  $V$  is a small perturbation. Then, we may

write the solution in the form of a rapidly converging Dyson series:

$$U(\phi, 0) = \sum_{l=0}^{\infty} U^{(l)}(\phi, 0), \quad (26)$$

where the  $l$ th terms  $U^{(l)}(\phi, 0)$  scales as the  $l$ th power of the perturbation.

The zeroth-order term  $U^{(0)}(\phi, 0)$  is defined as the evolution operator for zero perturbation. So we can evaluate this term analytically, we take  $H_0$  as the first term on the right-hand-side of (21) (proportional to  $\sigma_1$ ). It follows that

$$V(\phi) = (\kappa \sin 2\phi)\sigma_3, \quad (27)$$

and

$$\begin{aligned} U^{(0)}(\phi, 0) &= \exp\left(i \int_0^\phi d\phi' H_0(\phi')\right) \\ &= \exp\left[\frac{1}{2}i\sigma_1\left(\Delta_0\phi + \frac{1}{2}\Delta_1 \sin 2\phi\right)\right]. \end{aligned} \quad (28)$$

The first-order correction  $U^{(1)}(\phi, 0)$  is then given by [36]

$$U^{(1)}(\phi, 0) = i \int_0^\phi d\phi' U^{(0)}(\phi, \phi')V(\phi')U^{(0)}(\phi', 0). \quad (29)$$

Substituting  $V(\phi)$  and  $U^{(0)}$  from Eqs. (27) and (28), the integration in (29) can be performed by employing the Jacobi-Anger expansion [37]

$$\exp(iz \sin \theta) = \sum_{n=-\infty}^{\infty} J_n(z) \exp(in\theta), \quad (30)$$

where  $J_n(z)$  is the Bessel function of the first kind and integer order  $n$ , evaluated at  $z$ . After some algebra, we obtain

$$\begin{aligned} U^{(1)}(\phi, 0) &= i\kappa\phi \sum_{n=-\infty}^{\infty} W_n(\Delta_1) \text{sinc}[\phi(n + \Delta_0/2)] \\ &\quad \times (\sigma_2 \cos \chi_n - \sigma_3 \sin \chi_n), \end{aligned} \quad (31)$$

where

$$W_n(\Delta_1) \equiv [J_{n-1}(\Delta_1/2) - J_{n+1}(\Delta_1/2)]/2, \quad (32)$$

$$\text{sinc}(x) \equiv \begin{cases} \sin(x)/x, & \text{for } x \neq 0 \\ 1, & \text{for } x = 0, \end{cases} \quad (33)$$

and

$$\chi_n(\phi) \equiv \frac{1}{4}\Delta_1 \sin 2\phi - n\phi. \quad (34)$$

As is usual in quantum dynamics, we can neglect terms of order higher than one in the Dyson series (26) for a small perturbation  $V$ .

The most striking feature of Eq. (31) is the appearance of an infinite number of coupling resonances occurring when  $n + \Delta_0/2 = 0$  for some integer  $n$ . Each of these resonances is the product of three factors. One factor is the unitary matrix  $(\sigma_2 \cos \chi_n - \sigma_3 \sin \chi_n)$ . The second one is the sinc term representing the decrease in strength of the resonance as  $\Delta_0/2$  moves away from  $-n$ . This kind of dependence is typical for a quantum-mechanical system driven by a sinusoidal classical field [38]. The third factor is the weighting function  $W_n(\Delta_1)$ .

For  $\Delta_1 = 0$ ,  $W_n(0) = (\delta_{n,1} - \delta_{n,-1})/2$ , and the infinite sum reduces to only two terms with  $n = \pm 1$ . As  $\Delta_1$  moves away from zero, new resonances appear for other values of  $n$ . Even though the amplitudes of original two resonances decrease, they remain prominent for small values of  $|\Delta_1|$ .

As discussed in Sec. IV B,  $U(2\pi, 0)$  determines the ring's polarization eigenstates and the resonances of the microring resonator. From Eq. (28),  $U^{(0)}(2\pi, 0) = \exp(i\pi \Delta_0 \sigma_1)$ . From Eq. (31), the first-order term  $U^{(1)}(2\pi, 0)$  becomes proportional to  $\sigma_2$  because  $\chi_n = -2\pi n$  and the  $\sigma_3$  term vanishes. Furthermore, when  $\Delta_0$  is an integer,  $U^{(1)}(2\pi, 0)$  simplifies to

$$U^{(1)}(2\pi, 0) = \begin{cases} 0, & \text{for } \Delta_0 \text{ odd} \\ i2\pi\kappa\sigma_2 W_m(\Delta_1), & \text{for } \Delta_0 \text{ even,} \end{cases} \quad (35)$$

where  $m$  is the integer satisfying

$$\Delta_0 + 2m = 0. \quad (36)$$

So when  $\Delta_0$  is an odd integer, the first-order correction to the round-trip matrix  $U(2\pi, 0)$  vanishes and  $U(2\pi, 0) \approx \exp(i\pi \Delta_0 \sigma_1)$  to first order in  $V$ . In addition, note that even for fixed  $\Delta_1$  and  $\kappa$ , the maximum amplitude of  $U^{(1)}(2\pi, 0)$  does not necessarily align with even values of  $\Delta_0$ , as Eq. (35) seems to suggest. This is because, as  $\Delta_0$  moves away from  $-2m$ , the resonant term  $n = m$  diminishes in strength but the other terms of the infinite sum in (31) become nonzero and start to contribute to  $U^{(1)}(2\pi, 0)$ .

We briefly address the validity of the perturbative solution. We truncated the Dyson series in Eq. (26) to its first two terms. This series is known to converge rapidly when the perturbation  $V$  is small. From Eq. (27),  $V$  can be said to be small for any  $\phi$  only if  $\kappa$  is small. How small  $\kappa$  must be is a subtle question. A necessary condition is that the power transferred between the TE and TM modes must be negligible, i.e.,  $|U_{12}(\phi, 0)|^2 \ll 1$ . Assuming that  $W_n(\Delta_1) \approx 1$  for the coupling resonance with  $n$  closest to  $-\Delta_0/2$ , we get  $|\kappa| \ll 2$  as a necessary condition for the perturbative approximation to be valid.

#### D. Resonant regime

As we just saw, the modulation of level spacing induced by  $\Delta_1$  results in an infinite set of coupling resonances in the perturbative regime. It turns out that this conclusion holds even beyond the accuracy of the first-order perturbation [24]. When  $\Delta_0$  approximately satisfies Eq. (36) for some integer  $m$ , the  $m$ th resonance in Eq. (31) is most strongly excited. It follows that, if the coupling strength  $\kappa$  is small enough, it is justified to neglect all other coupling resonances, since only the  $m$ th resonance has its effect accumulate and become non-negligible as  $\phi$  varies from 0 to  $2\pi$ .

Under this approximation,  $U(\phi, 0)$  is found to be given by [24]

$$U(\phi, 0) \approx \exp[i\sigma_1 \chi_m(\phi)] \exp(i\phi H_{\text{RWA}}), \quad (37)$$

where  $\chi_m(\phi)$  is defined in Eq. (34) and the matrix  $H_{\text{RWA}}$  is given by

$$H_{\text{RWA}} = \frac{1}{2}(\Delta_0 + 2m)\sigma_1 + \kappa W_m(\Delta_1)\sigma_2, \quad (38)$$

with  $W_m(\Delta_1)$  defined in (32). The neglect of the nonresonant terms of  $H(\phi)$  is known as the rotating-wave approximation (RWA) in quantum mechanics [30].

Recalling from Eq. (34) that  $\chi_m(2\pi) = -2\pi m$ , we find

$$U(2\pi, 0) \approx \exp(i2\pi H_{\text{RWA}}). \quad (39)$$

Thus, the eigenvectors of  $H_{\text{RWA}}$  are approximately those of  $U(2\pi, 0)$ . After a round-trip, they each acquire a phase of  $\theta(2\pi) \pm \pi \Delta_{\text{RWA}}$ , where  $\theta(2\pi)$  is the common round-trip phase from Eq. (19) and  $\Delta_{\text{RWA}}$  is the difference between the eigenvalues of  $H_{\text{RWA}}$ . It is straightforward to verify that

$$\Delta_{\text{RWA}} = \sqrt{(\Delta_0 + 2m)^2 + 4\kappa^2 W_m^2(\Delta_1)}. \quad (40)$$

In particular, when (36) is nearly satisfied,  $H_{\text{RWA}}$  is close to proportional to  $\sigma_2$ , and its polarization eigenstates approximately correspond to the Jones vectors  $(1, 1)^T/\sqrt{2}$  and  $(1, -1)^T/\sqrt{2}$ . These are also approximately the polarization eigenstates of the round-trip matrix  $U(2\pi, 0)$ , if the RWA applies.

To understand these results, we note that, in the absence of coupling ( $\kappa = 0$ ), TE and TM modes are independent and acquire different phases after a round trip. When Eq. (36) is satisfied, they acquire the same phase (up to a multiple of  $2\pi$ ). Hence, a nonzero coupling lifts the phase-factor degeneracy and determines the eigenvector structure of  $U(2\pi, 0)$ .

We refer to the region where Eq. (36) approximately applies and  $|\kappa|$  is small enough for Eq. (37) to hold as the resonant regime. If  $|\kappa|$  becomes too large, the contributions to  $H(\phi)$  neglected in the RWA may noticeably alter the polarization dynamics, despite their effect not accumulating over  $\phi$ . This pair of conditions may appear stricter than those governing the perturbative regime, which requires only  $|\kappa|$  to be small. However, this is not the case because Eq. (37) is valid for values of  $|\kappa|$  larger than those for which (29) holds. To see this, note that the expression in Eq. (37) is unitary, while the two-term Dyson series  $U \approx U^{(0)} + U^{(1)}$  is not. This feature implies that Eq. (37) automatically conserves the total power  $a^\dagger a$ , while the sum  $U^{(0)} + U^{(1)}$  only approximately does so if  $|\kappa| \ll 2$ .

#### E. Adiabatic regime

In the adiabatic regime, if the polarization state  $a(\phi)$  is an eigenstate of the matrix  $H(\phi)$ , it continuously follows the local eigenstate of  $H(\phi)$  as  $\phi$  increases and  $H(\phi)$  varies. Let  $a^{(\pm)}(\phi)$  be the local eigenstates, i.e., the two Jones vectors satisfying the eigenvalue equation

$$H(\phi)a^{(\pm)}(\phi) = k_{\pm}(\phi)a^{(\pm)}(\phi), \quad (41)$$

with eigenvalues  $k^{(\pm)}(\phi)$  depending on  $\phi$ . The adiabatic theorem states that, in the limit  $|k_+(\phi) - k_-(\phi)| \rightarrow \infty$ ,  $U(\phi, 0)$  tends toward [36,39]

$$U_A(\phi, 0) = \sum_{n \in \{+, -\}} \exp \left[ i \int_0^\phi d\phi' k_n(\phi') \right] \times \exp [i\gamma_n(\phi)] a^{(n)}(\phi) [a^{(n)}(0)]^\dagger. \quad (42)$$

The argument of the first exponential in this expression is known as the dynamic phase. The argument of the second one,

$\gamma_n(\phi)$ , is the so-called geometric phase. In the adiabatic approximation [39],  $U(\phi, 0) \approx U_A(\phi, 0)$ . A good rule of thumb [33,36] for its validity is that the difference in eigenvalues should be much larger than the characteristic frequency at which  $H(\phi)$  changes. For our problem, this condition requires  $|k_+ - k_-| \gg 2$  from Eq. (21).

The calculation of the geometric phase  $\gamma_n(\phi)$  in Eq. (42) is generally cumbersome. Nevertheless, following Berry [31], we can evaluate its value when  $H(\phi)$  returns to its original value  $H(0)$ . For our microring resonator, this happens when  $\phi$  is an integer multiple of  $\pi$ . Applying Berry's general result, we may write [24]

$$\exp[i\gamma_{\pm}(\pi)] = \begin{cases} -1, & |\Delta_0| < |\Delta_1| \\ +1, & |\Delta_0| > |\Delta_1| \end{cases} \quad (43)$$

and

$$\exp[i\gamma_{\pm}(2\pi)] = \exp[i2\gamma_{\pm}(\pi)] = 1 \text{ for } |\Delta_0| \neq |\Delta_1|. \quad (44)$$

No expression for the geometric phase exists when  $|\Delta_0| = |\Delta_1|$ , because the adiabatic approximation does no longer hold in that case, as explained in Ref. [24].

Naturally, the round-trip matrix  $U(2\pi, 0)$  can be approximated with  $U_A(2\pi, 0)$  in the adiabatic regime. Additionally, it takes a substantially simpler form compared with the general expression in Eq. (42). To see this, recall from Eq. (21) that the eigenstates of  $H(0) = H(2\pi)$  are  $(1, 0)^T$  and  $(0, 1)^T$ . Also, it is easy to see that the trace of  $H(\phi)$  vanishes. Hence, its eigenvalues satisfy  $k_+(\phi) = -k_-(\phi) = \Delta(\phi)/2$  where  $\Delta(\phi)$  is the eigenvalue difference. From Eq. (21),  $\Delta(\phi)$  is readily found to be

$$\Delta(\phi) = \sqrt{[\Delta_0 + \Delta_1 \cos(2\phi)]^2 + 4\kappa^2 \sin^2(2\phi)}. \quad (45)$$

Using this result, one gets the simple expression

$$U_A(2\pi, 0) = \exp\left[\pm i\sigma_1 \int_0^\pi d\phi \Delta(\phi)\right]. \quad (46)$$

In (46),  $\pm$  is taken as “+” if the TE mode at  $\phi = 0$  has higher effective index than the TM mode and is taken as “-” otherwise.

So we find that, in the adiabatic regime, the ring's polarization eigenstates are always TE and TM polarizations. The net effect of the polarization coupling induced by  $\kappa$  is merely to alter the phase difference after a round-trip according to (45) and (46).

## VI. A PRACTICAL EXAMPLE

To illustrate the usefulness of our coupled-mode formalism, we examine a specific example and focus on a material platform based on LN [8]. More precisely, we model a microring resonator made with a waveguide whose LN core with silicon dioxide ( $\text{SiO}_2$ ) substrate and air cladding. The resonator is excited with a laser operating at the 1550 nm wavelength. At this wavelength, the ordinary and extraordinary refractive indexes of LN are  $n_o = 2.21$  and  $n_e = 2.14$ , respectively. Silicon dioxide is isotropic with a refractive index of 1.444 for this wavelength. Air is isotropic with a refractive index of unity. We consider waveguides of

different thickness, but for concreteness, we fix the ring radius to 100  $\mu\text{m}$ .

To observe interesting polarization dynamics,  $\Delta_0$  must be of the order of unity. Otherwise, the dynamics become adiabatic with local eigenstates never deviating far from fully TE and fully TM modes. This requirement on  $\Delta_0$  between the fundamental modes leads us to consider multimoded LN waveguides with thicknesses in the range of 0.7 to 1.0  $\mu\text{m}$ , in agreement with previous experimental work [8]. However, we neglect higher-order modes in our analysis and examine coupling only between the fundamental TE and TM modes. As mentioned in Sec. V A, this is legitimate if the difference in propagation constants between the fundamental and higher-order modes is much larger than the matrix elements  $\zeta D_{mn}^{(l)}$  of the perturbation, which we assume to be true. The validity of this assumption is verified in Sec. VI A.

### A. Local effective indices and comparison with finite-element calculations

To validate our coupled-mode description, we compare its predictions with those obtained with commercial numerical software. Specifically, we calculate the effective indices  $n_{\text{eff}}^{(+)}$  and  $n_{\text{eff}}^{(-)}$  for the two modes of the ring waveguide as a function of the  $\phi$  and use them to compute the angle-dependent polarization-averaged index  $\bar{n}_{\text{eff}} = (n_{\text{eff}}^{(+)} + n_{\text{eff}}^{(-)})/2$  and the modal birefringence  $B(\phi) = n_{\text{eff}}^{(+)} - n_{\text{eff}}^{(-)}$ . From our CMT, we have

$$B(\phi) = \Delta(\phi)/(k_0 r), \quad (47)$$

with  $\Delta(\phi)$  given by (45). In the absence of material birefringence,  $B(\phi)$  does not depend on  $\phi$  and reduces to the geometric birefringence due to mode confinement. In the presence of material anisotropy,  $B(\phi)$  varies with  $\phi$  and reveals key features of the polarization coupling, as we will see shortly. To evaluate  $\bar{n}_{\text{eff}}$ , we use Eqs. (18) and (19) to obtain

$$\bar{n}_{\text{eff}}(\phi) = \bar{\beta}(\phi)/k_0 = (k_0 r)^{-1} d\theta/d\phi, \quad (48)$$

where

$$\bar{\beta}(\phi) = \bar{\beta}_0 + \bar{\beta}_1 \cos 2\phi, \quad (49)$$

along with

$$\begin{aligned} \bar{\beta}_1 &= -\zeta (D_{ss}^{(1)} - D_{pp}^{(3)})/2, \\ \bar{\beta}_0 &= (\beta_s + \beta_p)/2 - \bar{\beta}_1. \end{aligned} \quad (50)$$

As stated, we want to compare the CMT results for  $\bar{n}(\phi)$  and  $B(\phi)$  with numerical values calculated with commercial software. We wish to show that our simplified CMT of polarization coupling, with Hamiltonian matrix (21), is legitimate not only for in-plane slab waveguides, but also for thin waveguides with a finite two-dimensional (2D) cross section. To do this, we evaluate the matrix elements  $D_{ss}^{(1)}$ ,  $D_{sp}^{(2)}$ , and  $D_{pp}^{(3)}$  for the TE and TM modes of ridge waveguides with fully 2D cross sections, assuming that they are wide enough for all other matrix elements to be comparatively negligible. We then calculate the parameters  $\Delta_0$ ,  $\Delta_1$ , and  $\kappa$  from Eq. (23) for in-plane slabs and calculate  $B(\phi)$  using (45) and (47) and  $\bar{n}_{\text{eff}}(\phi)$  using (48) and (49). For the numerical computations, we use the fully tensorial version of the finite-element method



(FEM) mode solver in Photon Design’s FIMMWAVE software suite.

The results are displayed in Fig. 3 (top and middle) over the half ring  $-\pi/2 \leq \phi \leq \pi/2$ . Only half of the ring need be considered because the local modes are periodic in  $\phi$  with period  $\pi$ , as evinced, for instance, by Eq. (15). In Fig. 3, CMT results are depicted with solid lines and FEM results are shown with circles. We consider ridge waveguides, all with a common thickness (height) of  $1 \mu\text{m}$  and ridge widths of 1.6, 1.8, and  $2.0 \mu\text{m}$ . For reference, we also depict  $\bar{n}(\phi)$  and  $B(\phi)$  for an in-plane slab with the same thickness of  $1 \mu\text{m}$ . We set  $1 \mu\text{m}$  for the thickness of the LN film because then  $\Delta_0 \approx 0$  for the in-plane slab at  $1550 \text{ nm}$  causing the effects of polarization coupling to be more evident. The bottom part of Fig. 3 shows an expanded view  $B(\phi)$  over a narrower range,  $\pi/6 \leq \phi \leq \pi/4$ . This auxiliary plot allows us to resolve the minima in  $B(\phi)$  around  $\phi = \pi/4$ . These minima are important because they reveal information about the coupling strength, as we elaborate below.

Figure 3 shows that there is close agreement between the CMT and the FEM curves for both  $\bar{n}(\phi)$  and  $B(\phi)$ . From this, we can draw two conclusions. First, we confirm that Eqs. (45) and (49) accurately predict the  $\phi$  dependence of  $\Delta(\phi)$  and  $\tilde{\beta}(\phi)$ , even for waveguides of two-dimensional cross section, so long as they are sufficiently thin. Second, we deduce that Eqs. (23) and (50) are accurate expressions for the parameters determining the local effective indices. Both conclusions support our CMT description of the polarization dynamics.

Note that the middle plot in Fig. 3, of  $B(\phi)$  over the half ring, is not useful to determine the coupling strength  $\kappa$ . This is because  $|\kappa/\Delta_1| \approx 0.01$  for our LN waveguides, so the effect of a nonzero  $\kappa$  is negligible everywhere except in the regions where  $(\Delta_0 + \Delta_1 \cos 2\phi) \approx 0$ . This occurs when  $\phi \approx \pm\pi/4$  because  $(\Delta_0/\Delta_1) \approx 0$ . Thus, we need to examine  $B(\phi)$  around  $\phi = \pm\pi/4$  to determine whether the CMT values for  $\kappa$  are accurate. This is why the bottom part of Fig. 3 is useful. The good agreement between the CMT and FEM values for  $B(\phi)$  in Fig. 3 (bottom) legitimizes the use of Eq. (23) for the coupling strength  $\kappa$  for our LN films.

In aggregate, the plots of Fig. 3 confirm that  $H(\phi)$  gives an accurate prediction for the local effective indices along the ring, despite neglecting coupling with higher-order modes, as argued in the opening paragraphs of this section. This is legitimate if the matrix elements  $\zeta D_{mn}^{(l)}$  inducing coupling are much smaller than the difference in propagation constants between modes of different order. In the evaluation of the local indices, this condition follows from quantum-mechanical stationary perturbation theory [19]. The good agreement between the CMT and FEM results shows that this neglect of higher-order modes is valid for the LN waveguides under consideration.

Observe that the in-plane slab curves for  $\bar{n}(\phi)$  and  $B(\phi)$  have generally the same shape as those for the ridge waveguides with finite width. However, the slab curves are noticeably distinct for the ridge widths considered. The  $\bar{n}(\phi)$  curve for the slab, in particular, is visibly offset from the three  $\bar{n}(\phi)$  curves for ridge waveguides. Nonetheless, this offset can be intuitively understood as a consequence of decreased

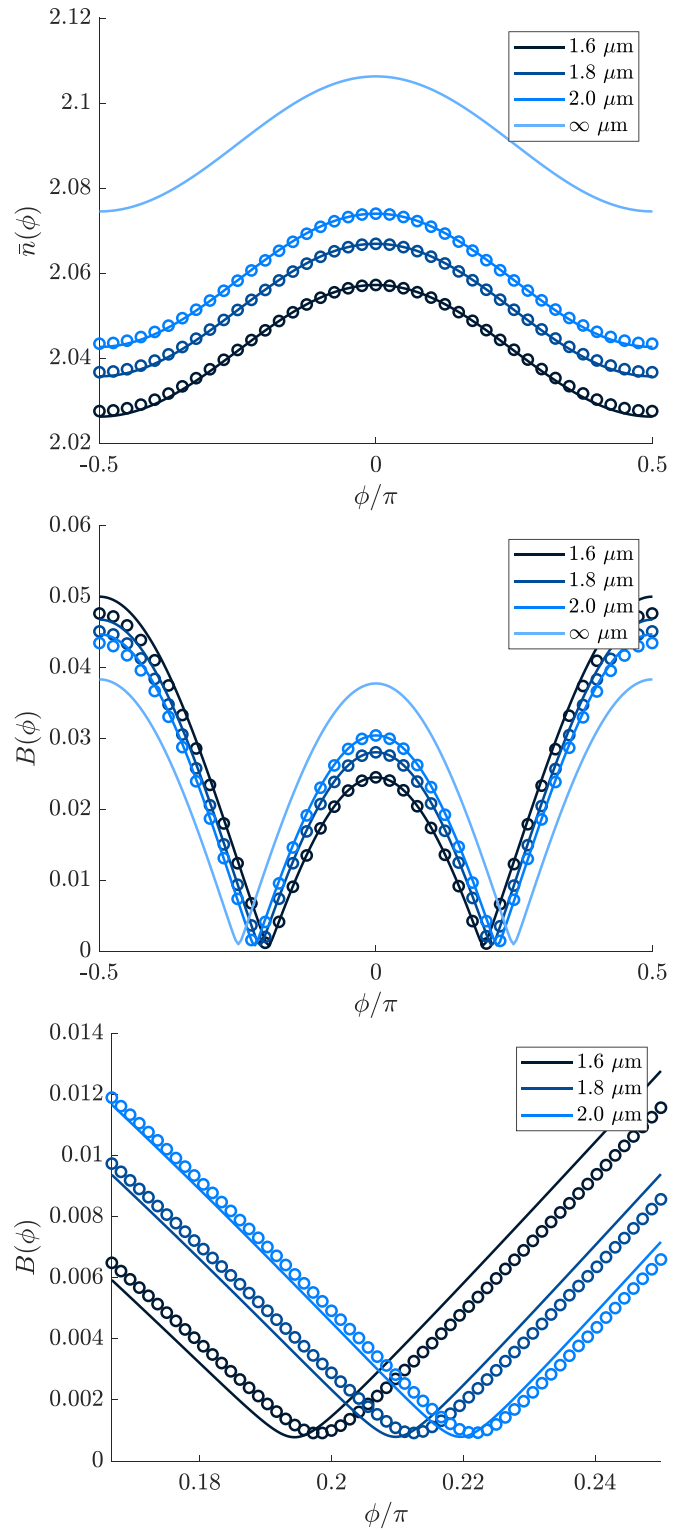


FIG. 3. Variation of the polarization-averaged effective index  $\bar{n}(\phi)$  (top) and the modal birefringence  $B(\phi)$  (middle) as a function of the microring angle  $\phi$  for different ridge waveguide widths. The bottom plot depicts  $B(\phi)$  in the neighborhood of the index anticrossings. Solid lines correspond to coupled-mode theory (CMT) results. Circles correspond to finite-element method (FEM) results.

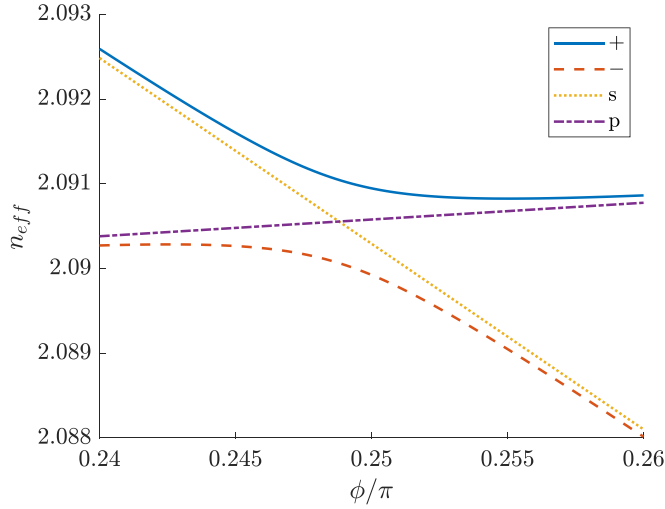


FIG. 4. Effective-index anticrossing in a LN microring resonator modeled as an in-plane slab with a thickness of  $1 \mu\text{m}$ . The solid line and dashed line show the effective indices of the two modes (+ and -, respectively) as a function of the ring angle  $\phi$ . The dotted curve and dash-dot line shows the indices of the hypothetical bare TE ( $s$  polarization) and TM ( $p$  polarization) modes, respectively, in the absence of polarization coupling ( $\kappa = 0$ ).

transversal confinement. Because the optical modes of the slab waveguide are less confined than those of a ridge waveguide but obey the same wave equation inside the core, they acquire a larger phase per longitudinal translation, i.e., they possess larger effective indices. This argument also explains the monotonic increase in  $\bar{n}(\phi)$  for fixed  $\phi$  and increasing ridge width in Fig. 3 (top).

In contrast, the difference between  $B(\phi)$  [Fig. 3 (middle)] for the slab waveguide and that for ridge waveguides is not as significant as that for  $\bar{n}(\phi)$  [Fig. 3 (top)]. Thus, even if it might be imprecise to use the an in-plane slab model to calculate the phase accumulated along the ring, it may still yield accurate predictions for the polarization dynamics.

In Fig. 3,  $B(\phi)$  approaches zero near  $\phi = \pm\pi/4$ . As explained above, it never vanishes because of the intermodal coupling due to  $\kappa$ , as can be verified from Eq. (45). Hence, we expect the effective indices to exhibit an anticrossing behavior, well-known in the context of quantum-mechanical two-level systems. Figure 4 shows this feature by plotting the effective indices of the eigenmodes of  $H(\phi)$  for the in-plane slab in the region near  $\phi = \pi/4$  in solid and dashed lines. For comparison, the dotted and dash-dot lines depict the effective indices of the “bare” TE and TM modes when the coupling is absent (i.e.,  $\kappa$  is artificially set to zero). The curves depict the typical anticrossing behavior of a two-level system [19]:  $n_{\text{eff}}^{(+)}$  starts close to  $n_{\text{eff}}^{(s)}$  for  $\phi < \pi/4$ , but deviates from it in a parabolic manner as  $\phi$  approaches the crossing point near  $\phi = \pi/4$ . After the crossing,  $n_{\text{eff}}^{(+)}$  asymptotically approaches  $n_{\text{eff}}^{(p)}$ . The opposite transition occurs for  $n_{\text{eff}}^{(-)}$ .

There are two reasons why an analysis of the anticrossing in Fig. 4 is worthwhile. First, one may use the anticrossing effect to estimate the coupling coefficient  $\kappa$  from numerical data. If  $H(\phi)$  has the form given in Eq. (21), the level-spacing minima (the anticrossing point) occur when

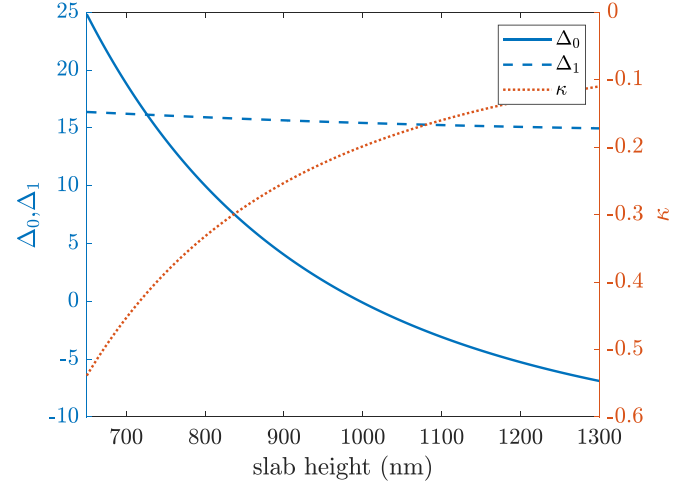


FIG. 5. Hamiltonian parameters plotted as a function of the waveguide thickness  $2d$ .

$2\phi = \pm\pi + \arccos[\Delta_0\Delta_1/(\Delta_1^2 + 4\kappa^2)]$ . To first order in  $\kappa$ , one finds that  $\Delta_{\min}$ , the value of  $\Delta(\phi)$  at these minima, is given by

$$\Delta_{\min} = 2|\kappa|\sqrt{1 - (\Delta_0/\Delta_1)^2}, \quad (51)$$

under the assumption that  $|\Delta_0/\Delta_1| \leq 1$ . Thus, one can use Eq. (51) to determine  $|\kappa|$  if  $\Delta_0$  and  $\Delta_1$  are known or if  $\Delta_0 = 0$ .

Second, examination of the anticrossings elucidates the nature of the local modes. For instance, from the proximity of  $n_{\text{eff}}^{(+)}$  to  $n_{\text{eff}}^{(s)}$  for  $\phi < \pi/4$  (and far from the intended crossing), we deduce that  $n_{\text{eff}}^{(+)}$  is a mostly  $s$ -polarized mode by a perturbation argument [19]. Similarly, we deduce that this mode becomes mostly  $p$  polarized after it passes the anticrossing. We also infer that the + mode is fully hybridized at the anticrossing. In fact, it can be regarded as circularly polarized, if the caveats outlined in Sec. VB are respected. This is easily verified by diagonalizing  $H(\phi)$  in Eq. (21) for  $\Delta_0 + \Delta_1 \cos(2\phi) = 0$ , as this is a necessary condition for the anticrossing to appear. These observations suggest that, if the ring radius  $r$  is large enough for the polarization dynamics to be adiabatic, one would observe  $s$ -polarized light become circularly polarized (again, recalling the caveats of Sec. VB) and then  $p$  polarized as it passes the anticrossing. Similarly,  $p$ -polarized light would become circularly polarized (of opposite handedness) and then  $s$  polarized as it traverses the anticrossing.

Note, though, that for this adiabatic evolution to occur, the adiabatic condition  $\Delta(\phi) \gg 2$  should hold for all  $\phi$ , so the minimum value  $\Delta_{\min}$  from Eq. (51) must satisfy  $\Delta_{\min} \gg 2$ . Conversely, this requires  $|\kappa| \gg 1$ . Since  $\kappa$  is proportional to the ring radius  $r$ , the adiabatic condition bounds  $r$  from below. For instance, we find in Sec. VIB, from Fig. 5, that  $|\kappa|$  is in the order of 0.3 for LN microrings with radius of  $100 \mu\text{m}$ . Thus, satisfying  $|\kappa| \gg 1$  for the same ring cross-section requires increasing  $r$  at least to  $1 \sim 3 \text{ mm}$ . This should still be experimentally feasible, although, as losses in LN waveguides have been reported to be in the order of  $0.1 \text{ dB/cm}$  [40].

### B. Influence of slab thickness

In this section, we analyze the effect of the waveguide's geometry on the Hamiltonian parameters  $\Delta_0$ ,  $\Delta_1$ , and  $\kappa$  and the concomitant polarization dynamics along a ring round-trip. Staying in the in-plane slab model, the only geometrical parameters to vary are the ring radius  $r$  and the slab thickness (or height)  $2d$ , keeping notation consistent with the Supplementary Material [24]. Given Eq. (23), it is clear that changes in the ring radius  $r$  only rescale the Hamiltonian matrix. Although such rescaling can change the polarization dynamics (say, by taking it from the resonant to the adiabatic regime), this change is easily predictable. For this reason, we keep the ring's radius fixed at  $100 \mu\text{m}$  and focus on the dependence of the polarization dynamics on the waveguide's thickness.

Figure 5 shows how the parameters  $\Delta_0$ ,  $\Delta_1$ , and  $\kappa$  vary as a function of  $2d$ . Both  $\Delta_0$  and  $\kappa$  vary appreciably as thickness is varied from 600 to 1300 nm;  $\Delta_0$  even changes its sign. The coupling parameter  $\kappa$  decreases in magnitude by a factor of five over this thickness range. In contrast,  $\Delta_1$  maintains a comparatively constant value of approximately 16 over the entire thickness range.

In particular, the large variation in  $\Delta_0$  from 25 to  $-5$  suggests drastic changes in the polarization evolution as  $2d$  varies from 600 to 1300 nm. Recall from Sec. VE that the evolution falls in the adiabatic regime when the eigenvalue difference  $\Delta(\phi)$  is large compared with two. It follows from Eq. (45) that this is the case when  $(|\Delta_0| - |\Delta_1|) \gg 2$ . Since this applies in the neighborhood of 600 nm, we expect the dynamics to fall in the adiabatic regime in this thickness range. As  $2d$  increases past 600 nm,  $\Delta_0$  rapidly decreases toward zero. Because we always have  $|\kappa| < 1$ , the decrease in  $|\Delta_0|$  causes the dynamics to leave the adiabatic regime because it is no longer true that  $\Delta(\phi) \gg 2$  for all  $\phi$ . The polarization dynamics are then susceptible to the excitation of coupling resonances when  $\Delta_0$  approaches an even integer, as discussed in Sec. VD. In the thickness range 800–1300 nm,  $|\Delta_0|$  has relatively small values, on the order of unity. Consequently, we expect the excited resonances to have non-negligible weights  $W_n(\Delta_1)$  and polarization coupling to be most pronounced when such resonances occur.

To verify these predictions, we solved the coupled-mode equations (20) numerically over one round trip with the initial condition that the pure TE (TM) mode is excited initially at  $\phi = 0$  for  $2d$  from 600 to 1300 nm. As  $\phi$  increases, the mode coupling leads to the transfer of power to the TM (TE) mode. We denote the fraction of power transferred as  $P_{sp}(\phi)$  and use it to calculate two quantities: the round-trip power (RTP),  $P_{sp}(2\pi)$  and the mean coupled power (MCP), i.e., the fraction of coupled power averaged over a round trip  $(2\pi)^{-1} \int_0^{2\pi} d\phi P_{sp}(\phi)$ . Because of the unitary evolution of the Jones vector along the ring, both the RTP and the MCP are independent of whether TE or TM light is injected at  $\phi = 0$ . Although both the RTP and the MCP are measures of the polarization hybridization, they provide different information. The RTP measures the net hybridization after one round trip and the hybridization of the ring's polarization eigenstates. On the other hand, the MCP is a global measure of the average hybridization over the ring.

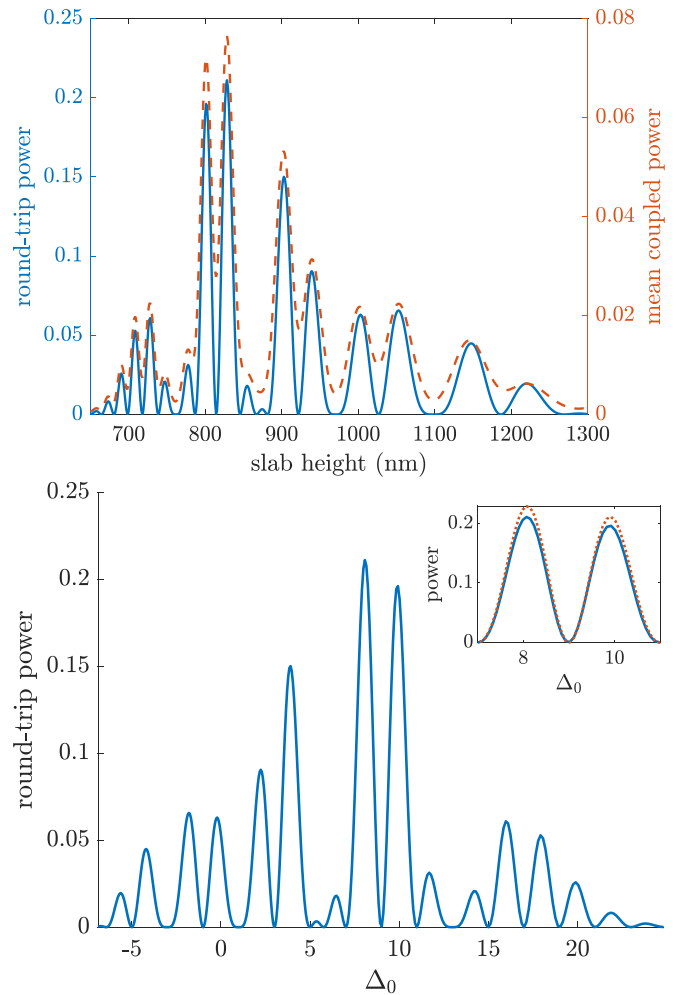


FIG. 6. Round-trip power (solid blue line) and mean coupled power (dashed orange line) as a function of slab height  $2d$  (top). Round-trip power as a function of  $\Delta_0$  (bottom). Inset compares the numerically calculated round-trip power (solid blue line) with that predicted by first-order perturbation (dotted orange line).

Figure 6 depicts the RTP and MCP as a function of  $2d$ . Both quantities exhibit multiple aligned peaks representing resonances. From the previous discussion, we expect these resonances to appear when  $\Delta_0$  approaches an even integer. The solid trace in Fig. 6 confirms this by plotting RTP as a function of  $\Delta_0$ . Even though the RTP peaks mostly align with even integer values of  $\Delta_0$ , the alignment is not perfect and deviates occasionally from Eq. (39). As explained in Sec. VC, such deviations are due to the effect of neighboring resonances on the polarization evolution. This can be verified through comparison of the numerically calculated RTP with that predicted by the perturbative formula (31).

As seen in the inset of Fig. 6, the perturbative calculation mostly retraces the RTP. The inset zooms into the  $\Delta_0 \approx 8, 10$  peaks so the difference between the numerical and perturbative RTP can be resolved. Small deviations arise only from a slight overestimation of the maxima's magnitudes. This difference is most pronounced for these two peaks because they are the largest in magnitude, but it exists for all the resonance peaks. The slight overshoot of the perturbative RTP

is explained by noting that the perturbative approximation  $U(2\pi, 0) \approx U^{(0)}(2\pi, 0) + U^{(1)}(2\pi, 0)$  neglects coupling saturation, i.e., it assumes the power of the launched TE or TM polarization is not depleted because of polarization coupling. The close agreement between the perturbative and numerical RTP and the location of the RTP minima at odd-integer  $\Delta_0$  values allows us to interpret the RTP minima as a consequence of Eq. (35). Thus, we verify that the slab thicknesses corresponding to odd-integer  $\Delta_0$  possess TE- and TM-polarized round-trip eigenstates.

Returning to the upper plot in Fig. 6, we note that the resonance peaks are tightly packed in the neighborhood of  $2d = 600$  nm and progressively spread out as  $2d$  increases. Inspecting Fig. 5, we can attribute this behavior to the fact that, although  $\Delta_0$  varies monotonically with  $2d$ , the variation is nonlinear. For smaller values of  $d$ ,  $\Delta_0$  changes more rapidly with  $d$ . This argument is confirmed in the lower trace. When we plot the RTP with respect to  $\Delta_0$ , the resonance valleys and peaks become evenly spaced.

### C. Polarization evolution along the microring

Our CMT can be used to study how an initial SOP evolves along the microring as it is affected by the competing geometrical and material birefringence. In this section, we analyze the polarization dynamics along the microring in the resonant and adiabatic regimes of the parameter-space and verify the validity of the approximate solutions given in Secs. VD and VE.

First, we investigate the resonant regime and fix the waveguide thickness at 800 nm, for which  $\Delta_0 \approx 10$ , and a coupling resonance results with  $m = -5$  (see Sec. VD). We numerically integrate the coupled-mode equations (20) with an initially TE-polarized mode  $[a(0) = (1, 0)^T]$  and plot the resulting Stokes vector  $\mathbf{S}(\phi)$ , with components  $S_j(\phi) = a^\dagger(\phi)\sigma_j a(\phi)$ , on the Poincaré sphere to track the evolution of the SOP. The resulting plot is presented in Fig. 7 (top). The numerically computed  $\mathbf{S}(\phi)$  is represented by the solid blue curve, while the behavior predicted by the RWA solution, obtained from Eq. (37), is drawn with a dashed orange curve.

Although the numerical and the RWA curves in Fig. 7 trace noticeably different trajectories on the Poincaré sphere, they both describe a similar overall nutation of the SOP away from the initial TE-polarization. This is seen in the lower plot of Fig. 7, where we plot the fraction of power transferred to the initially unexcited TM-polarization as a function of  $\phi$ , i.e.,  $P_{sp}(\phi)$  in the notation of Sec. VIB. It is evident that the RWA solution successfully describes the accumulating effect of the polarization coupling, while ignoring the small-mode-power oscillations of the numerical solution. These oscillations are associated with the off-resonant terms of the Hamiltonian matrix, which are neglected in the RWA.

Lastly, we examine a case where the polarization dynamics lie in the adiabatic regime by choosing  $2d = 500$  nm. In this case,  $\Delta_0 = 52.4$  and  $\Delta_1 = 16.6$ , hence  $\Delta(\phi) \geq (|\Delta_0| - |\Delta_1|) \gg 2$  for all  $\phi$ . Once again, we evaluate the fraction of power  $P_{sp}(\phi)$  coupled into the TM mode when the TE mode is excited at  $\phi = 0$ . Figure 8 presents  $P_{sp}(\phi)$  as computed from a numerical solution of Eq. (20) and compares it with the values predicted from the adiabatic approximation. Clearly,

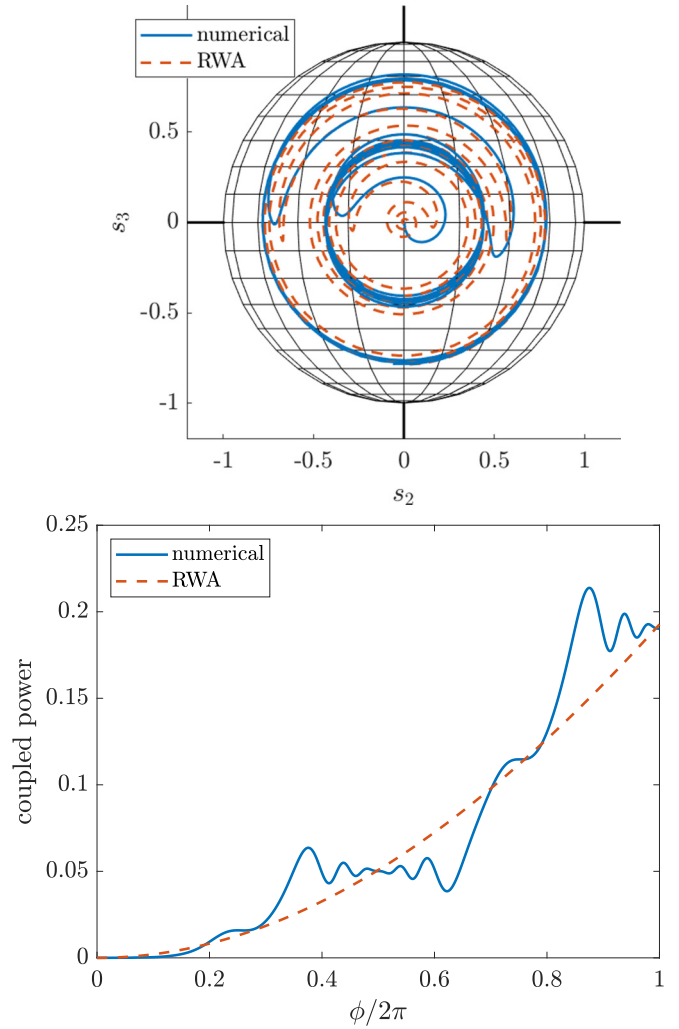


FIG. 7. Evolution of the SOP on the Poincaré sphere of initially  $s$ -polarized light for  $2d = 800$  nm (top). Fractional power transfer as a function of angle  $\phi$  (bottom). The solid blue trace shows the numerically evaluated evolution; the dashed orange trace shows the evolution under the RWA.

there is very good agreement between the two curves for all  $\phi$ . The only features that the adiabatic approximation does not reproduce are the rapid, small-amplitude oscillations on top of the accumulated power. These can be understood as artifacts of a finite (contrary to infinitely small) rate of change of the Hamiltonian matrix.

## VII. CONCLUSIONS

We developed a theoretical framework for studying the evolution of polarization inside a microring resonator whose waveguide has a core made with a uniaxial birefringent material. We introduced a zero-bending model that replaces the ring waveguide with a straight one but retain the continuous reorientation of the optic axis relative to the direction of propagation. We wrote Maxwell's equations in the form of a Schrödinger equation and used it to obtain the equations governing the resulting coupling between TE and TM polarizations.

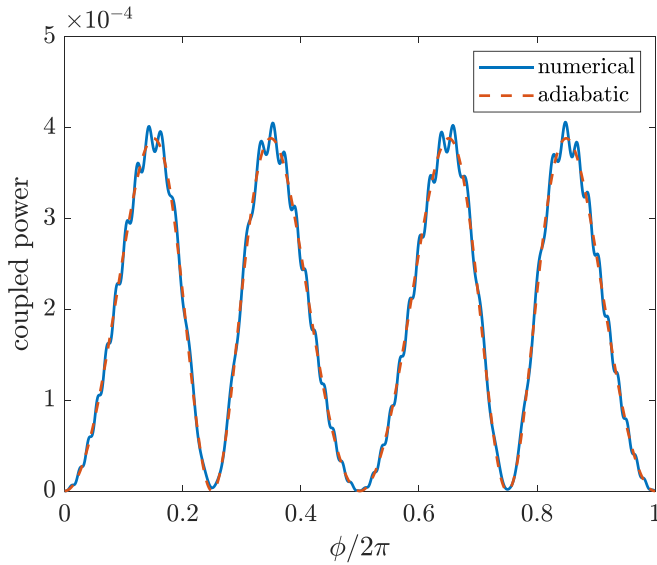


FIG. 8. Fraction of power coupled into the initially unexcited polarization for  $2d = 500$  nm, calculated numerically (solid blue line) and via the adiabatic approximation (dashed orange line).

We solved the coupled-mode equations in the simple case when only fundamental TE and TM modes are coupled due to the reorientation of the optic axis. We found that the resulting coupled-mode equations are identical to the Schrödinger equation of a two-level atom under optical excitation and external frequency modulation. We leveraged this isomorphism and used analytical tools from quantum mechanics to study the polarization dynamics inside the microring under different parameter regimes. Our formalism can be used to characterize the polarization properties of microrings made with a uniaxial material such as lithium niobate. The study of such microrings is of great technological importance, since they are the building block of many electro-optical and nonlinear optical devices.

#### ACKNOWLEDGMENTS

We acknowledge helpful discussions with K. Opong-Mensah at the early stages of this research. The work is supported by the National Science Foundation Grant No. ECCS-1807735. L.C.H. acknowledges financial support from Mexico's National Council of Science and Technology (CONACYT).

- [1] T. J. Kippenberg, R. Holzwarth, and S. A. Diddams, Microresonator-based optical frequency combs, *Science* **332**, 555 (2011).
- [2] S. A. Miller, Y. Okawachi, S. Ramelow, K. Luke, A. Dutt, A. Farsi, A. L. Gaeta, and M. Lipson, Tunable frequency combs based on dual microring resonators, *Opt. Express* **23**, 21527 (2015).
- [3] A. L. Gaeta, M. Lipson, and T. J. Kippenberg, Photonic-chip-based frequency combs, *Nat. Photonics* **13**, 158 (2019).
- [4] M. Zhang, C. Wang, R. Cheng, A. Shams-Ansari, and M. Loncar, Monolithic ultra-high-Q lithium niobate microring resonator, *Optica* **4**, 1536 (2017).
- [5] A. Rao and S. Fathpour, Heterogeneous thin-film lithium niobate integrated photonics for electrooptics and nonlinear optics, *IEEE J. Sel. Top. Quant. Electron* **24**, 1 (2018).
- [6] Y. He, H. Liang, R. Luo, M. Li, and Q. Lin, Dispersion engineered high quality lithium niobate microring resonators, *Opt. Express* **26**, 16315 (2018).
- [7] C. Wang, M. Zhang, M. Yu, R. Zhu, H. Hu, and M. Loncar, Monolithic lithium niobate photonic circuits for Kerr frequency comb generation and modulation, *Nat. Commun.* **10**, 978 (2019).
- [8] A. Pan, C. Hu, C. Zeng, and J. Xia, Fundamental mode hybridization in a thin film lithium niobate ridge waveguide, *Opt. Express* **27**, 35659 (2019).
- [9] D. P. Gia Russo and J. H. Harris, Wave propagation in anisotropic thin-film optical waveguides, *J. Opt. Soc. Am.* **63**, 138 (1973).
- [10] R. A. Steinberg and T. G. Giallorenzi, Modal fields of anisotropic channel waveguides, *J. Opt. Soc. Am.* **67**, 523 (1977).
- [11] D. Marcuse and I. P. Kaminov, Modes of a symmetric slab optical waveguide in birefringent media. Part II: Slab with coplanar optical axis, *IEEE J. Quantum Electron.* **15**, 92 (1979).
- [12] A. Knoesen, T. K. Gaylord, and M. G. Moharam, Hybrid guided modes in uniaxial dielectric planar waveguides, *J. Lightwave Technol.* **6**, 1083 (1988).
- [13] M. Lu and M. M. Fejer, Anisotropic dielectric waveguides, *J. Opt. Soc. Am. A* **10**, 246 (1993).
- [14] W. Liao, X. Chen, Y. Chen, Y. Xia, and Y. Chen, Explicit analysis of anisotropic planar waveguides by the analytical transfer-matrix method, *J. Opt. Soc. Am. A* **21**, 2196 (2004).
- [15] C. Vassallo, *Optical Waveguide Concepts* (Elsevier, Amsterdam, 1991).
- [16] S. G. Johnson, M. Ibanescu, M. Skorobogatiy, O. Weisberg, T. D. Engeness, M. Soljačić, S. A. Jacobs, J. Joannopoulos, and Y. Fink, Low-loss asymptotically single-mode propagation in large-core omniguide fibers, *Opt. Express* **9**, 748 (2001).
- [17] B. A. Daniel, Ph.D. thesis, University of Rochester, 2012, <http://hdl.handle.net/1802/21340>.
- [18] R. A. Sammut, Orthogonality and normalization of radiation modes in dielectric waveguides, *J. Opt. Soc. Am.* **72**, 1335 (1982).
- [19] C. Cohen-Tannoudji, B. Diu, and F. Laloe, *Quantum Mechanics* (Wiley, 1977).
- [20] D. Marcuse, *Light Transmission Optics* (Van Nostrand Reinhold, New York, 1982).
- [21] N. Morita and R. Yamada, Electromagnetic fields in circular bends of slab waveguides, *J. Lightwave Technol.* **8**, 16 (1990).
- [22] K. R. Hiremath, M. Hammer, R. Stoffer, L. Prkna, and J. Čtyrský, Analytic approach to dielectric optical bent slab waveguides, *Opt. Quantum Electron.* **37**, 37 (2005).
- [23] J. H. Shirley, Solution of the Schrödinger equation with a Hamiltonian periodic in time, *Phys. Rev.* **138**, B979 (1965).
- [24] See Supplemental Material at <http://link.aps.org/supplemental/10.1103/PhysRevA.103.063517> for complete mathematical expressions and derivations, which includes Refs. [25–33].

- [25] S. J. Orfanidis, *Electromagnetic waves and antennas*, 2014, <https://www.ece.rutgers.edu/~orfanidi/ewa/>.
- [26] A. Papoulis, *The Fourier Integral and its Applications*, McGraw-Hill electronic sciences series (McGraw-Hill, New York, 1962).
- [27] D. Marcuse, Modes of a symmetric slab optical waveguide in birefringent media - Part I: Optical axis not in plane of slab, *IEEE J. Quantum Elect.* **14**, 736 (1978).
- [28] L. Allen and J. H. Eberly, *Optical Resonance and Two-Level Atoms*, Vol. 28 (Wiley, New York, 1975).
- [29] G. B. Arfken and H.-J. Weber, *Mathematical Methods for Physicists*, 6th ed. (Elsevier, Boston, 2005).
- [30] M. P. Silveri, J. A. Tuorila, E. V. Thuneberg, and G. S. Paraoanu, Quantum systems under frequency modulation, *Rep. Prog. Phys.* **80**, 056002 (2017).
- [31] M. V. Berry, Quantal phase factors accompanying adiabatic changes, *Proc. R. Soc. Lond. A* **392**, 45 (1984).
- [32] A. Messiah, *Quantum Mechanics*, Dover Books on Physics (Dover Publications, 1999).
- [33] A. Aguiar Pinto, M. Nemes, J. Peixoto de Faria, and M. Thomaz, Comment on the adiabatic condition, *Am. J. Phys.* **68**, 955 (2000).
- [34] J. N. Damask, *Polarization Optics in Telecommunications* (Springer, New York, 2004), Vol. 101.
- [35] Q. Lin and G. P. Agrawal, Vector theory of four-wave mixing: Polarization effects in fiber-optic parametric amplifiers, *J. Opt. Soc. Am. B* **21**, 1216 (2004).
- [36] A. Messiah, *Quantum Mechanics*, Dover Books on Physics (Dover Publications, New York, 1999).
- [37] G. B. Arfken and H.-J. Weber, *Mathematical Methods for Physicists*, 6th ed. (Elsevier, Boston, 2005).
- [38] J. J. Sakurai and J. Napolitano, *Modern Quantum Mechanics*, 2nd ed. (Addison-Wesley, Boston, 2011).
- [39] D. J. Griffiths, *Introduction to Quantum Mechanics*, 2nd ed. (Pearson Prentice Hall, Upper Saddle River, 2005).
- [40] D. Zhu, L. Shao, M. Yu, R. Cheng, B. Desiatov, C. J. Xin, Y. Hu, J. Holzgrafe, S. Ghosh, A. Shams-Ansari *et al.*, Integrated photonics on thin-film lithium niobate, *Adv. Opt. Photonics* **13**, 242 (2021).